



1 **Characterization of the Newly Designed Wall-Free Particle Evaporator**
2 **(WALL-E) for Online Measurements of Atmospheric Particles**

3 Linyu Gao^{1,†}, Imad Zgheib^{1,#,†}, Evangelos Stergiou², Cecilie Carstens¹, Félix Sari Doré^{1,‡},
4 Michel Dupanloup¹, Frederic Bourgain¹, Sébastien Perrier¹, Matthieu Riva^{1*}

5 ¹ Univ Lyon, Université Claude Bernard Lyon 1, CNRS, IRCELYON, F-69626, Villeurbanne,
6 France

7 ² Environmental Chemical Processes Laboratory (ECPL), Department of Chemistry, University
8 of Crete, Voutes Campus, 70013 Heraklion, Greece

9 [#] now at TOFWERK, 3645 Thun, Switzerland

10 [‡] now at Department of Chemistry and Molecular Biology, Atmospheric Science, University of
11 Gothenburg, SE-41390, Gothenburg, Sweden

12 [†] These authors contributed equally to this work

13

14 Corresponding to: matthieu.riva@ircelyon.univ-lyon1.fr

15

16

17

18

19



20 Abstract

21 Organic aerosols (OA) play a critical role in the atmosphere by directly altering human health
22 and climate. Understanding their formation and evolution as well as their physicochemical
23 properties requires a detailed characterization of their chemical composition. Despite advanced
24 analytical techniques developed within the last decades, real-time online measurement of
25 atmospheric particles remains challenging and suffers from different artifacts. In this work, we
26 introduce the newly designed wall-free particle evaporator (WALL-E) coupled with a chemical
27 ionization mass spectrometer (CIMS) using bromide (Br^-) as the reagent ion. We
28 comprehensively evaluate the performance of the WALL-E system, demonstrating its ability to
29 evaporate particles while maintaining the integrity of the compounds composing the particles
30 (i.e., minimal thermal decomposition). To demonstrate WALL-E's performance, the
31 composition of aerosol particles formed from α -pinene ozonolysis in the presence of SO_2 is
32 characterized. In addition, by applying the scan declustering method, we can now provide a
33 quantification of the different species present in the condensed phase, e.g., $\text{C}_{10}\text{H}_{16}\text{O}_4$ 84 ng m^{-3}
34 3 , $\text{C}_{19}\text{H}_{28}\text{O}_7$ 7 ng m^{-3} for a total SOA mass of $1 \text{ } \mu\text{g} \cdot \text{m}^{-3}$. While dimers exhibit higher sensitivities,
35 they account for only 14-18% of the total particle masses, which is considerably lower than
36 their signal fractions (23-29%). This suggests a potential overestimation of the dimer
37 contributions when relying solely on signal fractions. In addition, volatility analysis using
38 thermograms reveals a clear relationship between T_{50} and compound saturation vapor pressure
39 (C^*), with lower-volatility species desorbing at higher temperatures. In addition, measured T_{50}
40 for α -pinene-derived SOA products agree well with theoretical volatility estimation models
41 (e.g., SIMPOL). Overall, this study demonstrates that WALL-E system coupled to a CIMS is a
42 promising technique for real-time particle characterization (i.e., composition, quantification,
43 and volatility) of atmospheric aerosols.



44 **1 Introduction**

45 Atmospheric organic aerosol (OA) particles play a critical role in the Earth's climate system
46 and atmospheric processes by affecting the radiative forcing, cloud formation and albedo,
47 atmospheric chemistry, environmental sustainability, and human health (Fehsenfeld et al., 1992;
48 Laothawornkitkul et al., 2009; Mellouki et al., 2015; Charnawskas et al., 2017). A large fraction
49 (20-90 %) of fine particles are comprised of OA (Kanakidou et al., 2005), which are estimated
50 to have a global source of 150 Tg yr⁻¹ (Pai et al., 2020). In the atmosphere, OA are either directly
51 emitted as particles from, e.g., volcanic eruption and biomass burning, or formed from gas-to-
52 particle conversion from the oxidation of volatile organic compounds (VOCs). Due to the
53 complex mixture of diverse organic compounds in OA particles, characterization of their
54 chemical composition remains challenging, notably at high time-resolution. Such
55 characterization is crucial for understanding particle formation, growth, aging, as well as their
56 physicochemical properties in the atmosphere. Therefore, improving online detection
57 techniques for OA particles is essential.

58 Currently, online mass spectrometry (MS), such as chemical ionization mass
59 spectrometer, is one of the key technologies for measuring gaseous oxygenated organic species.
60 It takes advantage of tracking the evolution of compounds during their formation and phase
61 partitioning. To retrieve particle-phase composition with a mass spectrometer, condensed
62 molecules must be converted to gaseous analytes before being ionized. The key point for getting
63 qualitative real-time particle composition information is the design of the inlet in front of the
64 MS. The current technologies to achieve this conversion can be broadly classified into two
65 categories: those requiring pre-collection of particles and those that do not. A thermal
66 desorption chemical ionization mass spectrometer (TD-CIMS) (Voisin et al., 2003; Smith et al.,
67 2004; Li et al., 2021) uses a metal filament in an electrostatic precipitator to collect pre-charged
68 aerosol particles and thereafter thermally evaporate them by pulsing a known current on the



69 filament. This approach requires both particle deposition and subsequent evaporation. Another
70 instrument involving particle collection is the filter inlet for gases and aerosols (FIGAERO)
71 developed by Lopez-Hilfiker et al. (2014). The FIGAERO inlet collects particles onto a PTFE
72 filter and desorbs them afterward using a heated N₂ flow. This approach enables the control of
73 particle evaporation in a pre-set temperature-ramping program, making it an efficient technique
74 to obtain particle volatility information (Stark et al., 2017; Bannan et al., 2019; Tikkanen et al.,
75 2020; Thornton et al., 2020) while reaching very low detection limits (Lopez-Hilfiker et al.,
76 2014; Thornton et al., 2020). However, since the collection and evaporation of aerosol particles
77 take several tens of minutes, the time resolution of particle measurements remains low,
78 especially in places with low particle loading, resulting in semi-online measurements. Because
79 of particle collection, the FIGAERO is also not interference-free from organic mixtures,
80 especially with high concentrations of aerosol particles (Bannan et al., 2019), which may affect
81 the retrieved volatility of single components. Finally, it has been shown that during evaporation,
82 chemical processes can occur, altering the chemical composition and the information retrieved
83 (Stark et al., 2017; Schobesberger et al., 2018; Buchholz et al., 2020).

84 In contrast, there are inlets without the need to pre-concentrate particles. An inlet
85 designed for chemical analysis of aerosols online (i.e., CHARON) has been developed without
86 the need to collect particles (Eichler et al., 2015). It consists of a carbon strip denuder for gas-
87 phase compound removal, an aerodynamic lens for particle collimation, and a thermo-
88 desorption unit for particle evaporation. The evaporated compounds can be analyzed with a
89 downstream low-pressure MS. However, due to the strong electric field in the ion drift tube,
90 the protonation-induced ionic fragmentation of oxygenated organic compounds biases the real
91 distribution of particle-phase chemical composition (Müller et al., 2017; Li et al., 2022; Peng
92 et al., 2023). Another technique, using an atmospheric pressure chemical ionization Orbitrap
93 mass spectrometer (APCI), evaporates aerosol particles in a heated ceramic tube where thermal



94 decomposition compounds can be observed (Vogel et al., 2016; Zuth et al., 2018). Finally, the
95 most recently developed vaporization inlet for aerosols (VIA) coupled to a NO₃-CIMS (VIA-
96 NO₃-CIMS) allows continuous thermal desorption and online detection of particle-phase highly
97 oxidized molecules without pre-concentration (Häkkinen et al., 2023). While this new coupling
98 allows the identification of highly oxygenated organic molecules at atmospheric relevant
99 particle concentration, the design of the VIA yields subsequent thermal fragmentation when the
100 analytes interact with the heated walls of the TD unit (Zhao et al., 2023; Zhao et al., 2024b).

101 To prevent thermal fragmentation, the extractive electrospray ionization time-of-flight
102 mass spectrometer (EESI-TOF-MS) (Lopez-Hilfiker et al., 2019) was developed as an online
103 method for particle analysis without the need of thermal desorption. In the EESI-TOF-MS,
104 sampled particles collide with charged electrospray droplets, and the soluble compounds are
105 extracted and ionized through adduct formation. However, the quantification of molecules
106 remains challenging due to the uncertainties in the dependence of instrument sensitivity on
107 molecular identity (Lopez-Hilfiker et al., 2019; Wang et al., 2021). This method exhibits also
108 important background due to the low selectivity of the reagent ions (e.g., Na⁺), making the
109 identification and the quantification of the compounds of interest challenging (Lee et al., 2020;
110 Bell et al., 2023).

111 In this work, a newly designed wall-free particle evaporator (WALL-E) is designed to
112 achieve real-time measurements of aerosol particles while preventing ionization-induced
113 fragmentation and minimizing thermal decomposition effects. WALL-E is coupled to a
114 chemical ionization inlet attached to a CIMS. An extensive characterization of the WALL-E
115 system is presented here, where its performance is tested as a function of various parameters,
116 e.g., flow rates and evaporation temperatures. The sensitivity of WALL-E coupled to an
117 atmospheric pressure CIMS is determined and the system is used to quantitatively retrieve the
118 composition of particle-phase oxygenated molecules generated from the O₃/OH initiated



oxidation of α -pinene in an aerosol flow tube reactor. Finally, by scanning the WALL-E temperature, volatility information can be extracted that can be inferred from the measured thermograms. Polyethylene glycol (PEG) is used to evaluate the volatility measurements and compare our results to the existing techniques.

2 WALL-E design, Experiments, and Instruments

2.1 WALL-E setup and simulations

The WALL-E system is designed to thermally desorb aerosol particles while minimizing the analyte wall-interactions with the system, thus limiting fragmentation (Figure 1). The system enables real-time mass spectrometric analysis of aerosol particles by integrating a series of carefully designed components, including a gas-phase denuder, a thermal desorber (TD) unit equipped with a sheath flow, a ceramic spacer for thermal isolation, and a dilution/cooling unit. Each component is optimized to enhance sample stability and compatibility with different types of CIMS.

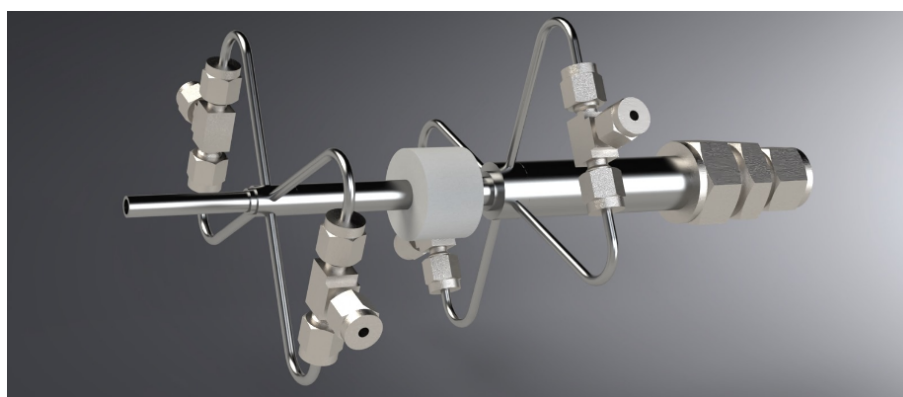


Figure 1. Design of the WALL-E interface.



136 **2.1.1 Gas-phase denuder**

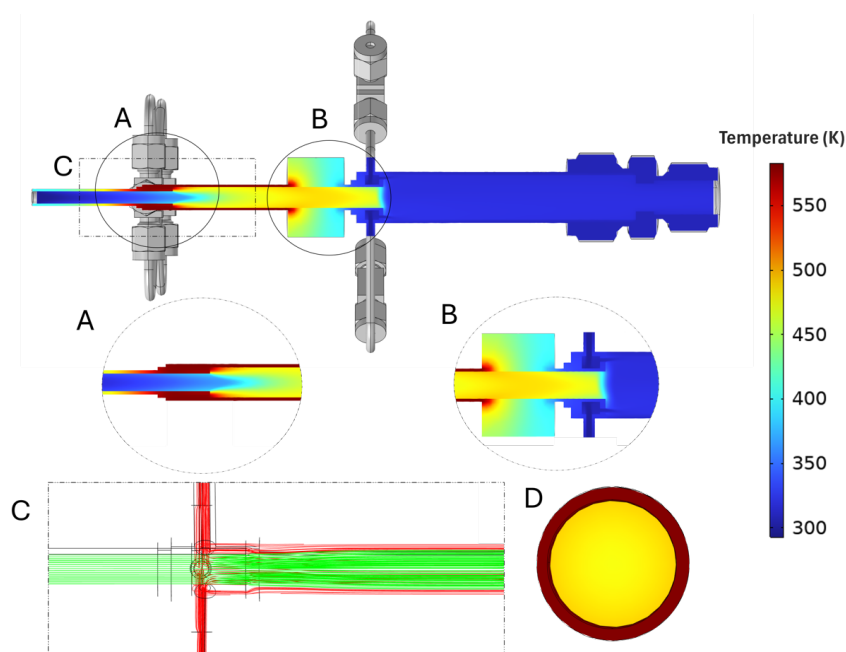
137 Like the EESI or the VIA design, the gas-phase denuder is the first stage of the WALL-E
138 system, designed to selectively remove VOCs and other inorganic gaseous species (e.g., nitric
139 acid) while allowing aerosol particles to pass through with minimal losses (transmission
140 efficiency > 90%). This denuder consists of a 10 mm outer diameter, 6 mm inner diameter,
141 stainless steel tube lined with an activated charcoal honeycomb structure, which provides a high
142 surface area for adsorption. Maintaining laminar flow is critical for the denuder's efficiency.
143 With a sample flow rate of 1 SLPM (standard liters per minute), the flow remains laminar with
144 a Reynolds number of 239, ensuring optimal gas-phase diffusion to the adsorbent walls.

145 **2.1.2 Core vaporization unit**

146 The TD is the core of WALL-E, where aerosol particles are converted into gas-phase species
147 through flash evaporation. It comprises a 4 cm stainless steel tube heated to up to 390°C. As
148 the sample flow enters the TD region, it merges with a hot nitrogen (N₂, up to 390°C) sheath
149 flow, introduced upstream at a flow rate ranging from 0 to 1 SLPM. The hot sheath-flow serves
150 multiple purposes: it maintains a laminar flow by preventing turbulences due to T differences
151 of the sampling flow with the walls of the TD and protects the evaporated analytes from the
152 heated walls. Hence, the TD's design prioritizes minimal wall interactions to reduce potential
153 fragmentation of the products, while ensuring that particle evaporation occurs within a well-
154 defined thermal environment. The stainless-steel tube provides consistent heat transfer along
155 its length, creating a stable thermal zone for the analytes. The combination of the heated tube
156 and the hot sheath-flow allows the aerosol particles to rapidly reach the target temperature,
157 significantly reducing the residence-time required for complete desorption. This rapid
158 temperature-ramp is essential for achieving flash evaporation, where particles are quickly
159 vaporized without prolonged exposure to high temperatures that could lead to thermal
160 decomposition.



161 Numerical simulations using COMSOL Multiphysics® are used to evaluate and refine
162 the flow and temperature dynamics within the system, employing models for turbulent flow,
163 compressible flow, heat transfer, and chemical transport. These simulations show the system's
164 ability to maintain laminar flow conditions across all units, which is essential to achieve
165 uniform heating and consistent particle transport. Experimental validation is performed in
166 conjunction with these simulations, offering valuable insights into both the operational
167 efficiency and areas for future optimization. The numerical simulations indicate the presence
168 of uniform heating along the tube length, with thermal stabilization achieved within the first
169 centimeter (Figure 2, section A). These simulations highlight a well-defined temperature
170 gradient that optimizes the desorption processes by ensuring a uniform thermal environment
171 throughout the TD. The combination of controlled flow rates, precise heating, and minimized
172 wall-interactions results in efficient aerosol evaporation with minimal fragmentation (Figure
173 2).



174



175 Figure 2: Composite simulation results of the WALL-E system focusing on the thermal
176 desorber (TD) part. A: Temperature profile in the first hot dilution mixing region, showing
177 efficient heat transfer and controlled mixing. B: Thermal isolation effectiveness of the ceramic
178 spacer. C: Streamlines in the sample and TD region, confirming laminar flow. D: Radial
179 temperature distribution at the TD exit, showing uniform heating across the sample flow.

180 **2.1.3 Dilution/cooling unit**

181 After the flash evaporation, a dilution/cooling flow is used by introducing nitrogen (room
182 temperature) via the second dilution region to prevent re-condensation of vaporized species.
183 This dilution unit is also a critical step to reduce turbulences caused by temperature gradients
184 between the TD and the downstream regions as previously observed with the VIA-CIMS
185 system (Zhao et al., 2024b). A ceramic spacer is positioned between the TD and the cooling
186 unit to ensure thermal isolation. This spacer, made from Alumina Ceramix Al_2O_3 with low
187 thermal conductivity, minimizes heat transfer between the heated TD and the cooled sample
188 stream, maintaining distinct thermal zones, as depicted in Figure 2. Simulations confirm the
189 effectiveness of the ceramic spacer in preserving thermal gradients, greatly reducing unwanted
190 heat transfer into the cooling unit. To further optimize the cooling unit, two fans are mounted
191 right after the second dilution region to ensure that the sample reaches room temperature while
192 preventing turbulence within the CI inlet. This separation is critical to ensure the stability of the
193 sample as it progresses toward the CI inlet operated at atmospheric pressure. As indicated in
194 Figure 2, the cooling seems to be achieved within the first centimeter while minimizing
195 turbulence.

196 **2.2 Experiments**

197 **2.2.1 Characterization of the optimal WALL-E setting parameters**



198 To determine the optimum WALL-E parameters (sampling flow rate, hot sheath-
199 flow/temperature, and TD temperature), particles are generated using an atomizer (Model 3076,
200 TSI, Minnesota, USA) with an aqueous solution of citric acid (Sigma-Aldrich, $\geq 99.5\%$), d-(+)-
201 glucose (Alfa Aesar, $\geq 99\%$), malonic acid (Sigma-Aldrich, 99%), phthalic acid (Sigma-Aldrich,
202 $\geq 99.5\%$), and ammonium sulfate (Sigma-Aldrich, $\geq 99\%$). Aerosol particles are dried using a
203 silica gel dryer, after which the sampling line is divided to provide an aerosol flow to a scanning
204 mobility particle sizer (SMPS, TSI Incorporated, USA) and to the WALL-E CIMS. The setup
205 is illustrated in Figure S1 and all parameters tested are summarized in Table S1.

206 2.2.2 Sensitivity determination

207 The sensitivity of individual compounds is directly proportional to their clustering strength with
208 the reagent ions (Iyer et al., 2016; Bi et al., 2021), which can be probed by performing a
209 declustering scanning procedure (Lopez-Hilfiker et al., 2016). Using the setup shown in Figure
210 S1, single component aerosol particles are generated using an atomizer containing single
211 component aqueous solutions of the following compounds: 1,5-dihydroxynaphthalene (Sigma-
212 Aldrich, $\geq 97\%$), 3,4,5-trihydroxybenzaldehyde (Sigma-Aldrich, $\geq 98\%$), 4-
213 hydroxyphenylacetic acid (Sigma-Aldrich, $\geq 98\%$), ammonium sulfate (Sigma-Aldrich, $\geq 99\%$),
214 citric acid (Sigma-Aldrich, $\geq 99.5\%$), d-(+)-glucose (Alfa Aesar, $\geq 99\%$), d-mannitol (Sigma-
215 Aldrich, $\geq 98\%$), phthalic acid (Sigma-Aldrich, $\geq 99.5\%$), phthalic acid d4 (Sigma-Aldrich,
216 $\geq 98\%$), and shikimic acid (Alfa Aesar, $\geq 98\%$). The sensitivity, reported in Table S2, for each
217 type of particle is determined by the linear regression of the mass concentration measured by
218 the SMPS and the normalized signal intensity of the analyte clustered with Br^- (i.e., $[\text{M}-\text{Br}]$)
219 detected by the WALL-E-CIMS (Figure S2). To further assess the correlation between the
220 sensitivity and the binding energy of the detected ion adducts, voltage scanning (i.e., increasing
221 the voltage difference between two ion optics) is performed to determine the half-signal



222 maximum intensity (Lopez-Hilfiker et al., 2016; Riva et al., 2020) for the generated single-
223 component aerosol particles.

224 2.2.3 SOA particle generation

225 To further examine the performance of the WALL-E system, SOA are generated in an 18-liter
226 Pyrex glass aerosol flow tube reactor (12 cm i.d. \times 158 cm length) from the O₃/OH initiated
227 oxidation of α -pinene in the presence of SO₂ at room temperature and atmospheric pressure
228 (Stein and Scott, 1994). Ozone (O₃) is stably generated by passing a flow of 0.6 SLPM of
229 synthetic air after exposure to a UV lamp (Ozone Generator Model 610, Jelight Company, Inc,
230 Irvine, USA). SO₂ is injected from a commercial cylinder (500 ppm, AIR PRODUCTS Inc.).
231 α -Pinene was introduced from a pressurized cylinder (40 ppm in nitrogen). O₃, SO₂, and α -
232 pinene are continuously injected into the aerosol flow tube reactor to generate a total aerosol
233 mass ranging from 1.0 to 15.6 $\mu\text{g}\cdot\text{m}^{-3}$. The concentrations of reactants are summarized in Table
234 S3. A mixture of nitrogen and oxygen (total flow 4 SLPM) is used as a carrier gas, providing a
235 reaction time of \sim 4.5 minutes. Before injecting α -pinene, background measurements are
236 obtained.

237 2.2.4 Thermograms and T_{max} determination

238 The volatility distribution of aerosol particles is investigated using thermograms obtained with
239 the WALL-E system. Polyethylene glycol (PEG-400) aerosols are produced by atomizing
240 aqueous solutions as performed in previous studies (Ylisirniö et al., 2021; Zhao et al., 2024b)
241 and sampled by the WALL-E system. The temperature of the WALL-E TD is gradually
242 increased from 30°C to 390°C in 30°C increments every 10 minutes. The PEG standards,
243 ranging from PEG-6 to PEG-17, have been chosen to represent a wide range of molecular
244 weights and volatilities (Krieger et al., 2018).

245



246 **2.3 Instrumentation**

247 Within these experiments, WALL-E is associated with an atmospheric pressure CI inlet (Riva
248 et al., 2019a; Riva et al., 2020) coupled to an Orbitrap (Q-Exactive, Thermo Fisher Scientific)
249 utilizing bromide ions (Br^-) as the reagent ion. Br^- is generated from dibromomethane (Sigma-
250 Aldrich, 99%) continuously flushed by 2 standard cubic centimeters per minute (sccm) of pure
251 N_2 , and subsequently ionized with a soft X-ray photoionizer (Hamamatsu, L9491). The sheath
252 and the total flows are 24 SLPM and 33.5 SLPM, respectively. The Orbitrap is operated with
253 an automatic gain control (AGC target) of 1×10^6 charges, an S-lens radio frequency level of
254 50, a maximum injection time of 1000 ms, 10 microscans, and a capillary temperature set to
255 150 °C. The mass resolution is 140,000 (at m/Q 200). Orbitool 2.2.4 (Cai et al., 2021) is used
256 for analyzing the data. The data are pre-averaged to 1 minute. Signals are background subtracted
257 and normalized by the signal intensity of Br^- (m/Q 79). To obtain an accurate concentration of
258 compounds present in low abundance, a linearity correction (Riva et al., 2020) is applied to all
259 measured signals (Figure S3).

260 The mass concentration of particles is retrieved using a scanning mobility particle sizer
261 (SMPS) utilizing a differential mobility analyzer (DMA; 3081, TSI Inc.) connected to a CPC
262 (3772, TSI Inc.), by applying an assumed particle density (1.45 g/cm^3) (Kim et al., 2010;
263 Shilling et al., 2009) for aerosol particles generated from the O_3/OH initiated oxidation of α -
264 pinene in the presence of SO_2 . An impactor (0.071 m) is used, and the sampling flow rate is 1
265 SLPM with a sheath flow of 10 SLPM.

266 **3 Results and Discussion**

267 **3.1 Optimal setting parameters of WALL-E**

268 As described in section 2.1, WALL-E involves multiple operational parameters, including the
269 sample flow rate (SF), the hot sheath flow rate (HF) and its temperature upstream of the TD,



the dilution flow in the cooling region, and the TD temperature region. The cooling flow is held constant at 10 SLPM to minimize turbulence in the CI inlet operated at atmospheric pressure. To determine the optimized parameters, various combinations of SF and HF flowrates as well as HF and TD temperatures are tested on aerosol particles generated from an atomized water solution containing a mix of standards. All data are corrected for their respective dilution factors. Figure 3 shows the summed signal of all evaporated products (i.e., phthalic acid, citric acid, malonic acid, glucose, sulfuric acid) under these different conditions, normalized to the maximum value.

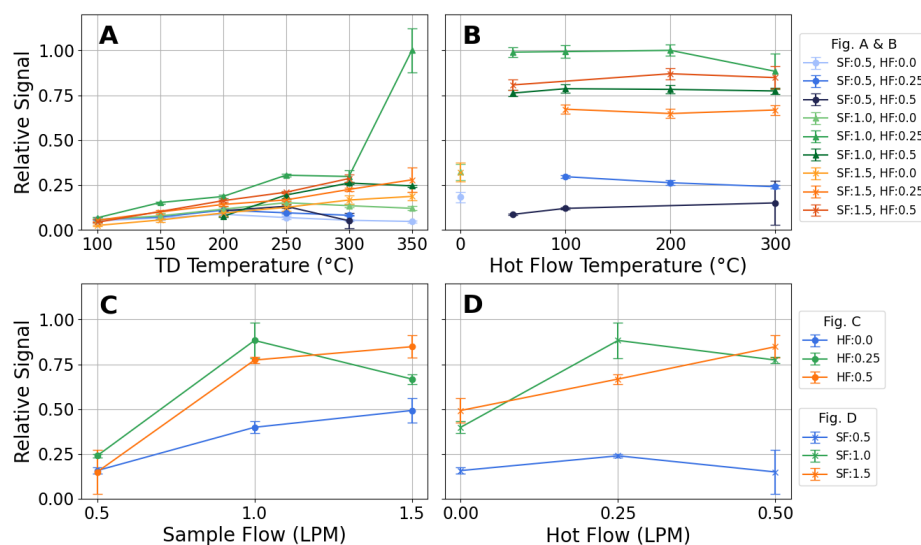


Figure 3: (A) Relative signal at a fixed hot sheath-flow (HF) temperature of 300 °C versus TD temperature for various combinations of sample flow rate (SF) and HF. (B) Relative signal at a fixed TD temperature of 300 °C versus HF temperature. (C) Relative signal versus SF at different HF settings. (D) Relative signal versus HF at different SF values. Both (C) and (D) are at a fixed TD and HF temperature of 300 °C. SF is the sample flow rate delivered to the TD, while HF is the heated dilution flow added upstream of the ambient dilution stage. The second, ambient dilution flow and the downstream cooling flow remain fixed to minimize turbulence



285 in the CIMS. Error bars represent standard deviations based on repeated measurements at the
286 same conditions, and all values are corrected for their respective dilution factors.

287 As depicted in Figure 3A, it is evident that a SF of 1.0 L min^{-1} consistently results in higher
288 signals than 0.5 L min^{-1} across all TD temperatures. A SF of 1.5 L min^{-1} also performs
289 reasonably well, whereas the 0.5 L min^{-1} configurations exhibit significantly lower signals. A
290 similar trend is observed in Figure 3B, where the relative signal is plotted against the HF
291 temperature. The results indicate that efficient evaporation occurs at a TD temperature of
292 around $300\text{--}350^\circ\text{C}$, while variations in the HF temperature have a less important effect.
293 However, the presence of a HF (either 0.25 or 0.5 L min^{-1}) at an SF of 1 or 1.5 L min^{-1} enhances
294 evaporation efficiency and flow stability. This influence of flow conditions is more distinctly
295 observed in Figures 3C and 3D and further illustrates the impact of SF and HF on the relative
296 signal. Figure 3C presents the relative signal as a function of SF for different HF settings,
297 demonstrating that a SF of 1 L min^{-1} and a HF of 0.25 L min^{-1} yield higher signal intensities
298 compared to other conditions. Similarly, Figure 3D shows the relative signal plotted against HF
299 at different SF values, reinforcing this observation.

300 A key consideration when selecting optimal SF and HF conditions is to keep
301 fragmentations minimal. Excessive heating in the TD can enhance fragmentation, potentially
302 resulting in thermal decomposition of the analytes. To assess this, we evaluate the thermal
303 decomposition of citric acid, which is a known analyte to decompose within TD inlets (Yang
304 et al., 2023). As shown in Figure S4, the thermal fragmentation of citric acid using the
305 conditions (i.e., SF of 1 L min^{-1} and a HF of 0.25 L min^{-1}) described above remains negligible,
306 with up to 2% of the total signal attributed to fragment ions at the hottest temperature (i.e.,
307 390°C). This confirms the minimal fragmentation while keeping an effective evaporation.

308



309 3.2 Characterization of SOA derived from α -pinene ozonolysis

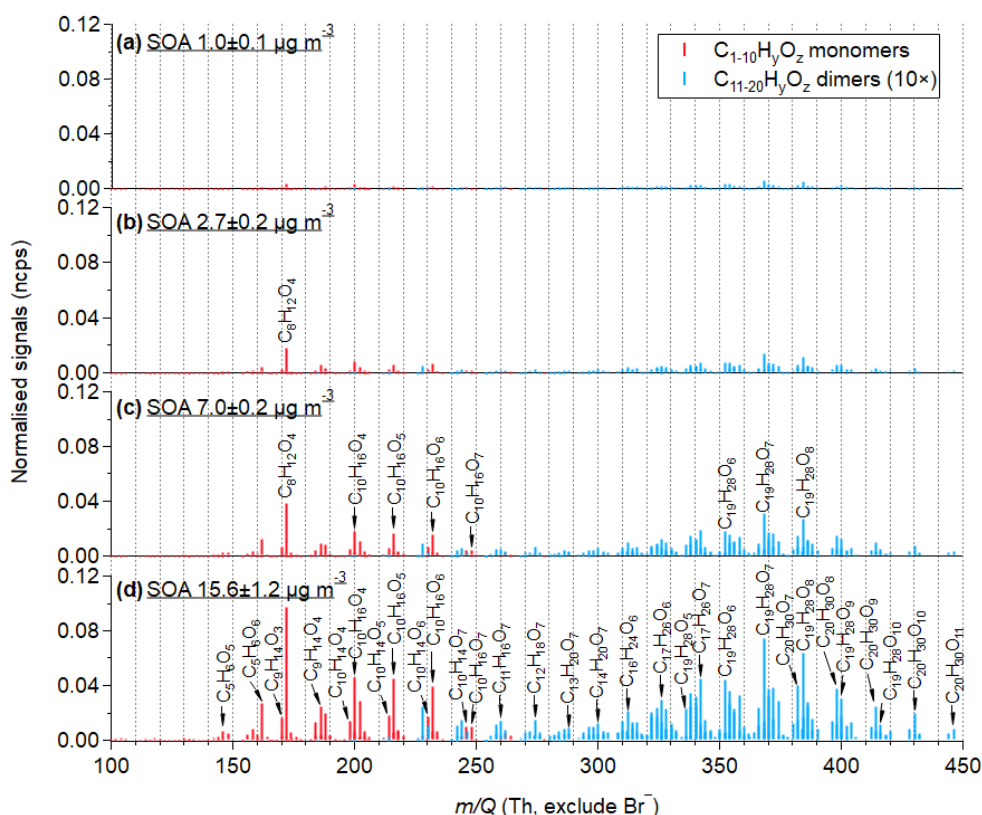
310 3.2.1 Raw mass spectra

311 To underline the performance of WALL-E in measuring and quantifying a complex mixture of
312 OA, the characterization of SOA generated from the oxidation of α -pinene in the presence of
313 SO_2 is used as an example. Figures 4 and S5 present the mass spectra of α -pinene-derived SOA
314 with particle mass concentrations ranging from 1.0 to 15.6 $\mu\text{g m}^{-3}$. These mass concentrations
315 cover atmospherically relevant ranges observed in remote and rural places (Jimenez et al., 2009),
316 which is achieved when using the optimal setting parameters determined in section 3.1. A total
317 of 146 organic monomers ($\text{C}_{1-10}\text{H}_y\text{O}_z\text{S}_0$) and 206 dimers ($\text{C}_{11-20}\text{H}_y\text{O}_z\text{S}_0$) are identified,
318 respectively contributing 67-74 % and 29-23 % to the total signal intensity. The dominant ions
319 identified in the monomer region are assigned to $\text{C}_{8-10}\text{H}_{12-18}\text{O}_{3-7}$ compounds with high-
320 resolution peak fitting in the range of m/Q at 249-343 Th, and $\text{C}_{17-20}\text{H}_{26-34}\text{O}_{5-11}$ compounds in
321 the dimeric range between 405-525 Th. Among the monomers, $\text{C}_{10}\text{H}_{14,16}\text{O}_{3-7}$ are the most
322 abundant ones, followed by $\text{C}_9\text{H}_{14}\text{O}_{3-7}$. The product distribution measured is consistent with
323 previous studies (Zhang et al., 2015; Kahnt et al., 2018; Zhao et al., 2023; Zhao et al., 2024a).
324 It should be mentioned that $\text{C}_8\text{H}_{12}\text{O}_4$ is the most abundant individual compound, which could
325 be norpinic acid or terpenylic acid identified by previous studies (Zhang et al., 2015; Du et al.,
326 2022; Witkowski et al., 2023). It has an unexpected high background of ~ 0.04 ncps when there
327 is no VOC injected. Desorption from the walls of the aerosol flow tube reactor when aerosol
328 particles are produced can explain the presence of $\text{C}_8\text{H}_{12}\text{O}_4$ as reported in previous laboratory
329 studies (Riva et al., 2019b; Wong et al., 2022).

330 Without sensitivity correction, compounds are significantly detected at a total signal of
331 0.04 ncps when the particle mass is $1.0 \pm 0.1 \mu\text{g m}^{-3}$. As particle mass concentration increases,
332 the normalized signals of particle-phase products also rise, reaching 0.8 ncps at $15.7 \pm 1.2 \mu\text{g m}^{-3}$.
333 The detected products exhibit a strong linear response to particle mass concentration, as



334 shown in Figure S6 illustrating the suitability of the WALL-E system at measuring aerosol
335 particles under atmospheric relevant conditions.



336

337 Figure 4. Mass spectra of particle-phase organic compounds formed from the oxidation of α -
338 pinene under varying mass particle concentrations ($1.0\text{--}15.6\ \mu\text{g}\cdot\text{m}^{-3}$). Compounds are
339 evaporated and detected by the WALL-E CIMS with HF and TD temperatures of $300\ ^\circ\text{C}$, SF of
340 1 SLPM, HF of 0.25 SLPM, and a cold dilution flow of 10 SLPM. Signals are normalized to
341 Br^- signal intensity. Red and blue refer to monomers ($\text{C}_{1-10}\text{H}_y\text{O}_x$) and dimers ($\text{C}_{11-20}\text{H}_y\text{O}_x$),
342 respectively. The normalized signals of dimeric compounds are multiplied by a factor of 10.

343

344



3.2.2 Sensitivity determination on SOA molecules

The sensitivity of standard compounds, which is determined by the linear regression between the normalized signals detected by WALL-E and the particle mass concentrations (Figure S2), is summarized in Table S2. The r^2 -values of the fitting for most standard compounds are good (0.93-0.99), while 1,5-dihydroxy naphthalene has the lowest r^2 -value of 0.85. By utilizing the in-source collision ion dissociation feature (Riva et al., 2019a), which corresponds to an increase in the DC offset voltages between two ion optics within the flatapole, the binding energy of the $[M-Br^-]$ adducts of the different compounds can be probed (Figure S7). Their dV_{50} values broadly range from 5.1 to 20.2 Volts, indicating differences in binding energies and varying clustering strengths to Br^- . Consequently, the correlation between the sensitivity and the dV_{50} values obtained from the standard compounds is fitted by a non-linear sigmoidal function (Figure S8), which is consistent with prior studies using the same approach to quantify gaseous species (Lopez-Hilfiker et al., 2016; Iyer et al., 2016; Zaytsev et al., 2019; Xu et al., 2022). This calibration curve provides an estimation of the system sensitivity based on experimentally obtained dV_{50} cluster values from declustering scans with increasing energy (Lopez-Hilfiker et al., 2019). Using this method, raw MS signal intensities can be converted into quantified amounts, reducing the need for compound-specific calibration when authentic standards are not available. This method enables semi-quantification across a wide variety of molecules.

By applying the correlation between sensitivity and dV_{50} obtained from the different standard compounds, and using the dV_{50} values determined for individual α -pinene-derived SOA products, every oxidation compound can be quantified. As an example, Figure S9 presents the declustering profiles of C_{10} monomers and C_{19-20} dimers from SOA. Consistent with previous studies (Riva et al., 2019a), more oxidized compounds exhibit stronger binding energies, resulting in higher dV_{50} values. As shown in Figure S10, the corresponding sensitivity



370 of α -pinene-derived SOA compounds generally increases with molecular mass and reaches a
371 plateau corresponding to the maximum sensitivity (i.e., collision limit), with an upper limit of
372 sensitivity of $0.08 \text{ ncps} \cdot \text{per} \cdot \mu\text{g} \cdot \text{m}^{-3}$.

373 3.2.3 Sensitivity-corrected chemical composition of SOA particles

374 By assessing the sensitivity of individual α -pinene-derived SOA compounds, the mass
375 concentrations of all identified particle-phase oxidation products can be estimated (Figure S11).
376 Using the correlation between sensitivity and dV_{50} based on 10 standard compounds, the total
377 particle mass concentration is estimated to be $27.1 \mu\text{g} \cdot \text{m}^{-3}$, 74% higher than the SMPS
378 measurements ($15.6 \mu\text{g} \cdot \text{m}^{-3}$), assuming spherical particles with an aerosol density of 1.45 g/m^3
379 (Kim et al., 2010; Shilling et al., 2009). By excluding the two outliers (i.e., shikimic acid and
380 glucose), the estimate of total particle mass concentration (with 36% overestimation) is closer
381 to the total particle mass concentration measured by the SMPS as depicted in Figure 5. As
382 discussed in previous studies, selected standard compounds might induce uncertainty in the
383 sensitivity estimations (Zaytsev et al., 2019; Bi et al., 2021; Song et al., 2024). Notably, the
384 presence of different isomers can yield substantial uncertainties, especially when their
385 sensitivity may vary by an order of magnitude (e.g., Lee et al., 2014). It should also be
386 mentioned that the total mass concentration determined by the SMPS is prone to uncertainties
387 (Wilson et al., 2015; Bell et al., 2023). Using the dV_{50} method presented here and considering
388 a total SOA mass of $15.1 \mu\text{g} \cdot \text{m}^{-3}$, the mass concentration of H_2SO_4 is estimated at $8.7 \mu\text{g} \cdot \text{m}^{-3}$
389 (using 10-compound fitting) and $6.4 \mu\text{g} \cdot \text{m}^{-3}$ (using 8-compound fitting). Comparing with the
390 direct calibration discussed above (i.e., Table S2), a good agreement is retrieved (7%
391 underestimation and 25% overestimation for the 10 and 8-compounds fit, respectively)
392 underlining the benefit of using this approach to obtain the concentrations of organic and
393 inorganic present in the particles. Overall, a linear relationship exists with the total SOA mass
394 concentrations in the range of $1.0\text{-}15.6 \mu\text{g} \cdot \text{m}^{-3}$ (Figure 5) and exhibits an overall good



agreement between WALL-E and SMPS measurements (i.e., 20-30%). Hence, this method can provide a deeper understanding of aerosol composition and evolution. For example, due to their general higher sensitivities, dimers contribute only 14-18% to the total mass (Figures 5, S10), much less than their fractions based on signal intensity (23-29%). This suggests that the dimer contributions to particles may be overestimated when solely based on signal intensity.

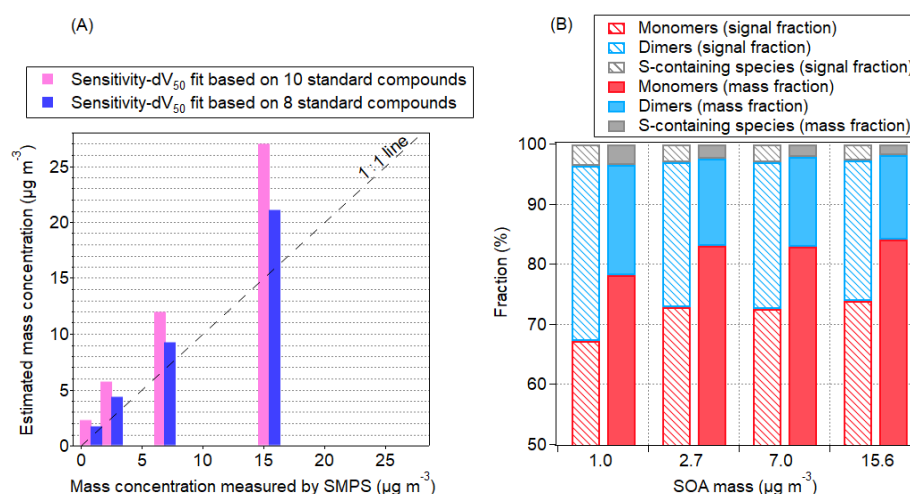


Figure 5. (A) The estimated mass concentration measured by Wall-E as a function of SOA mass concentration measured by the SMPS. (B) Fractions of monomers, dimers and sulphur-containing compounds in the SOA particles formed from O_3/OH initiated oxidation of α -pinene in the presence of SO_2 . The calculation of fractions is weighted by normalized signals (dashed bars) and mass concentrations (solid bars), respectively.

3.3 Assessing particle molecular volatility

3.3.1 Thermograms and T_{max} determination

The determination of volatility represents one of the greatest analytical challenges when characterizing aerosol particles, as it depends on multiple factors, including molecular composition, intermolecular interactions, and experimental conditions (Compernelle et al., 2011). Various experimental and theoretical techniques have been developed over the last



decades to retrieve volatility information, each with advantages and limitations. Filter-based techniques and thermal desorbers provide direct measurements of desorption profiles, while theoretical models, such as SIMPOL and COSMO-RS, offer predictive estimates of volatility based on molecular structure. However, volatility determination remains not well constrained, particularly for highly oxygenated and multifunctional compounds, where structural differences, such as isomerism, can significantly influence volatility (Lee et al., 2014; Bannan et al., 2019).

While FIGAERO and VIA have been widely used, their design constraints introduce inherent limitations. FIGAERO, being a filter-based technique, can introduce artifacts such as recondensation, analyte interactions, and fragmentation. The prolonged residence time on the filter may also lead to early desorption of volatile species or chemical reactions between co-deposited compounds, impacting the accuracy of volatility estimates (Stark et al., 2017; Schobesberger et al., 2018; Buchholz et al., 2020). VIA thermograms, on the other hand, show evidence of fragmentation and thermal decomposition at high temperatures (Zhao et al., 2024b). WALL-E introduces a new approach, optimizing the balance between thermal residence time and evaporation efficiency, allowing for precise volatility determination with reduced wall interactions.

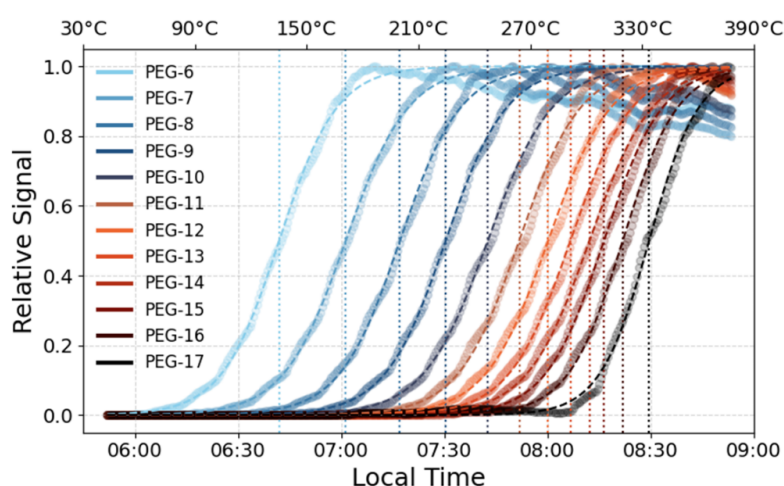
3.3.2 From T_{\max} to T_{50}

The T_{\max} values, which correspond to the peak desorption temperature, represent the temperature at which the maximum desorption rate occurs. Traditionally, T_{\max} has been used to estimate volatility from thermograms. This approach is well-suited for FIGAERO and VIA, where the thermograms typically exhibit a near-Gaussian profile, with a clear peak followed by a steep signal decline due to decomposition and fragmentation. However, in the case of WALL-E, where thermograms more closely follow a sigmoidal desorption trend, T_{\max} determination



436 becomes less straightforward. At high temperatures, the signal does not drop sharply but instead
437 asymptotically reaches a plateau, making T_{\max} highly sensitive to noise and minor variations in
438 the upper temperature range.

439 To overcome this limitation, we propose using T_{50} , the temperature at which the signal
440 reaches 50% of its maximum as a more robust volatility metric. Since T_{50} is located in the
441 steepest region of the sigmoid fit, it is significantly less affected by noise, baseline shifts, or
442 small variations in signal intensity. Unlike T_{\max} , which depends on the choice of an arbitrary
443 threshold (e.g., 99.5% or 99.9% of the signal maximum), T_{50} is a main feature of the sigmoid
444 function, making it a more consistent and reproducible parameter for comparing volatility
445 trends in the case of WALL-E. To accurately determine T_{50} , the thermograms are smoothed and
446 fitted using a sigmoid function. This approach minimizes the influence of temperature ramping
447 increments and instrumental noise. Figure 6 displays thermograms for PEG standards,
448 illustrating that less volatile compounds require higher temperatures for complete evaporation,
449 whereas more volatile compounds evaporate at lower temperatures.



450 Figure 6: Thermograms of PEG standards obtained using WALL-E. The desorption profiles
451 illustrate the relative signal intensity as a function of temperature.



452 The use of a sigmoid fit for the WALL-E data is justified by the observed thermograms, which
453 closely resemble this behaviour, with only a moderate signal decrease at the highest tested
454 temperatures. For comparison purposes with other particle evaporators, T_{\max} is used with a
455 signal representation of 98%. Figure S12 shows the effect of varying this signal percentage
456 threshold. By varying between 99.5% and 98%, a difference of about 10% in the T_{\max} value is
457 observed, which makes it challenging to select an appropriate threshold. In addition, at higher
458 temperatures, the fit for less volatile PEGs can result in more errors due to fewer data points.
459 Taking a threshold around where the signal is half always results in more accurate results even
460 with 10% variations in the threshold. The signals of more volatile compounds, such as PEG-6
461 and PEG-7, with T_{\max} values of 203.6°C and 246.3°C, decrease by only 11.2% and 18.9%
462 respectively, even after a temperature increase of over 150°C, which represents a significant
463 improvement compared to other online TD techniques. At this point, PEG-16 and PEG-17 reach
464 their T_{\max} (Table S4). This demonstrates WALL-E's ability to maintain signal integrity across
465 a wide volatility range, ensuring reliable thermal desorption without excessive signal loss.

466 3.3.3 Temperature Correction and Comparison with VIA and FIGAERO

467 The temperatures applied during thermal desorption in WALL-E do not directly reflect the
468 actual gas-phase temperatures experienced by the desorbed compounds. Due to thermal lag and
469 heat transfer dynamics, a correction factor was derived based on the COMSOL CFD
470 simulations. The internal gas temperature at the core of the TD was found to follow a linear
471 relationship with the set temperature (Figure S13). This correction ensures that the reported
472 T_{\max} values accurately represent the true volatility behaviour of the analytes. The corrected and
473 uncorrected T_{\max} values for each PEG compound are plotted against their molecular masses in
474 Figure S14. The corrected values align well with those reported for VIA and FIGAERO,
475 maintaining a consistent trend across different molecular weights. In contrast, the uncorrected
476 T_{\max} values are systematically higher, displaying a different slope compared to the other two



477 systems. This highlights the necessity of applying the correction factor to ensure accurate
478 volatility determination.

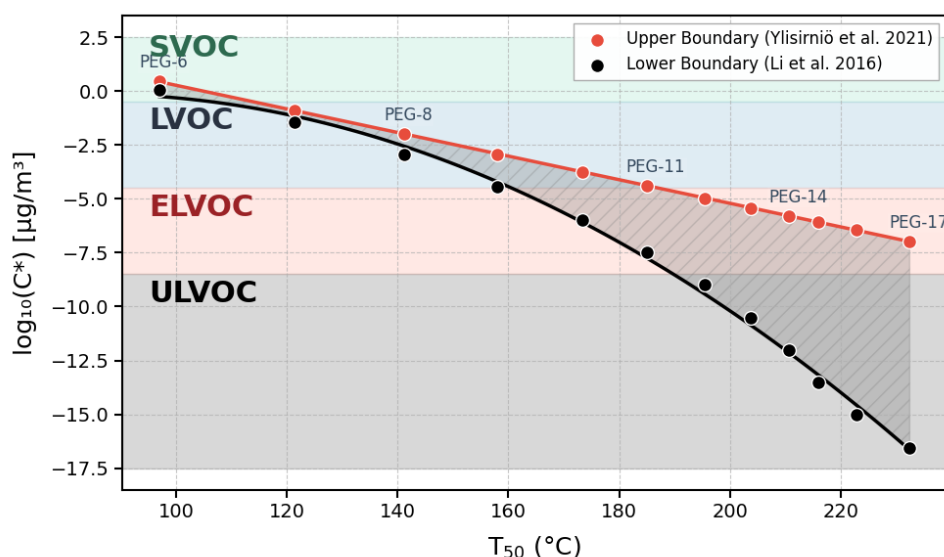
479 T_{\max} values from WALL-E and VIA are higher compared to FIGAERO, which can be
480 attributed to the short residence time in the TD region (Zhao et al., 2024b). Additionally,
481 WALL-E exhibits lower T_{\max} values than VIA, likely due to the introduction of heated dilution
482 flow into the sample stream. This promotes flash evaporation, causing compounds to desorb
483 before reaching full thermal equilibrium, ultimately shifting T_{\max} to lower values while
484 maintaining the expected volatility trend. As illustrated in Figure S15, the residence time in the
485 TD region further influences T_{\max} values. Longer residence times allow for gradual heating and
486 equilibration, leading to higher T_{\max} values. In contrast, shorter residence times accelerate
487 desorption, resulting in lower T_{\max} values due to insufficient thermal equilibration.

488 3.3.4 Volatility Estimation from T_{50}

489 As previously explained, the use of T_{50} would provide a more reliable estimation of the volatility,
490 which is typically inferred using the relationship between T_{50} and the saturation concentration
491 (C^*) as discussed in prior studies (Ylisirniö et al., 2021). The wide range of T_{50} values observed
492 for PEG standards underscores the broad applicability of WALL-E for volatility
493 characterization across diverse classes of compounds. To derive volatility estimates, we apply
494 the parameterization method proposed previously (Krieger et al., 2018; Ylisirniö et al., 2021),
495 which utilizes measured vapor pressures for PEG-5 to PEG-8 and extrapolates the trend for
496 higher molecular weights. Additionally, an alternative approach using the parameterization (Li
497 et al., 2016) is considered. While both methods produce similar trends for lower-mass PEGs,
498 they diverge significantly at higher masses, reflecting the inherent uncertainties in extrapolating
499 volatility predictions. Given these discrepancies, we define a volatility range (Figure 7) that



500 encompasses both parameterizations, providing a more robust estimation framework until
501 additional direct vapor pressure measurements become available.



502 Figure 7: Volatility estimation using measured T_{50} values, ranging from SVOC to ULVOC.

503 To assess the applicability of T_{50} -based volatility determination, we apply this approach to α -
504 pinene derived SOA compounds, specifically $C_{10}H_{16}O_{6-9}$. The T_{50} values of these SOA species
505 are determined using multiple ramp-up speeds, ensuring reproducibility across different heating
506 rates. Additionally, a faster temperature ramp-down from 390°C to 30°C is used as an
507 independent validation method. As shown in Figure 8, the T_{50} estimated using WALL-E for the
508 $C_{10}H_{16}O_{6-9}$ from the heating and cooling phases (i.e., temperature ramping up and down,
509 respectively) exhibit a very good agreement confirming the robustness of the system.

510 Determined T_{50} values are further compared with theoretical volatility estimation
511 models, specifically COSMO-RS and SIMPOL, as presented previously (Kurtén et al., 2016;
512 Peräkylä et al., 2020). Our measured T_{50} values for the SOA compounds fall well within the
513 SIMPOL-predicted region, confirming that the volatility estimates obtained using WALL-E are
514 consistent with theoretical predictions. As mentioned earlier, without a pre-separation method,



the presence of isomers can alter the quantification of the compounds of interest, which is also the case for volatility estimation. As previously discussed by Kurtén et al. (2016) and Peräkylä et al. (2020), isomeric structures can exhibit significantly different volatilities, reinforcing the need to account for molecular configurations beyond elemental composition when interpreting volatility trends.

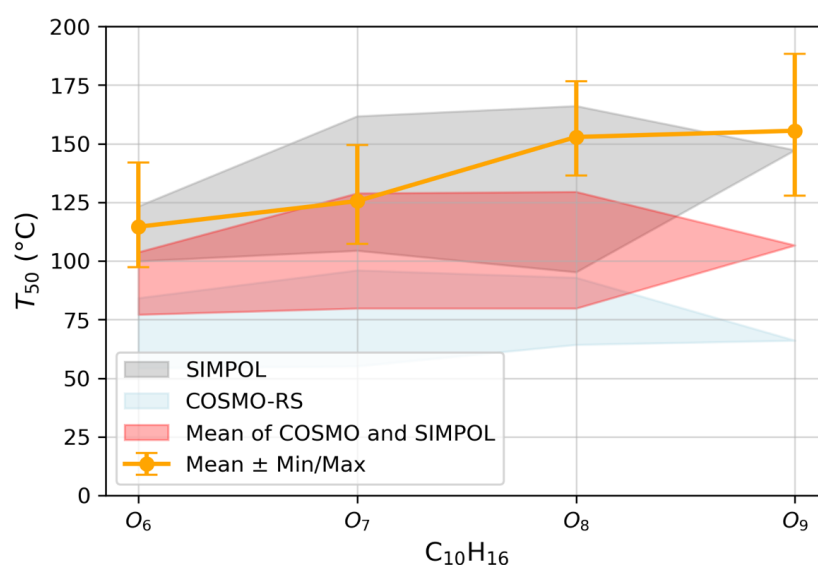


Figure 8: Comparison of estimated T_{50} values for α -pinene derived SOA compounds, specifically $C_{10}H_{16}O_{6-9}$ with volatility predictions from COSMO-RS and SIMPOL models. The measured T_{50} values (orange) are shown with their min/max range, while the shaded regions represent model predictions taking into consideration the isomerisation.

4 Conclusions

Within this work we present a new analytical method (i.e., WALL-E) to retrieve the chemical composition of atmospheric particles in real time. Coupled with a CIMS using Br^- ion chemistry as the reagent ion, WALL-E is comprehensively characterized, achieving efficient particle evaporation with maximum evaporation efficiency while exhibiting minimal thermal decomposition across a range of operational settings. The characterization of SOA produced



530 from the O₃/OH initiated oxidation of α -pinene in the presence of SO₂ further validates WALL-
531 E's performance in resolving and quantifying complex organic aerosol mixtures. It successfully
532 identifies a broad range of monomeric (C₁₋₁₀) and dimeric (C₁₁₋₂₀) compounds. By utilizing the
533 in-source collision ion dissociation feature, the sensitivity of the analytical method is realized
534 using a wide variety of authentic standards used to determine the correlation between binding
535 energy and sensitivity. By using this function and performing declustering procedures,
536 individual α -pinene derived SOA compounds are quantified at concentration as low as 10 pg·m⁻³
537 (for a total SOA mass of 1 $\mu\text{g}\cdot\text{m}^{-3}$). The total estimated SOA mass concentrations is in good
538 agreement with particle concentration measurements obtained by an SMPS, demonstrating the
539 benefit of this approach. Notably, the mass contribution of dimeric compounds is determined,
540 which reveals that they account for only 14-18% of total particle mass, which is notably lower
541 than their fractions (23-29%) based on signal intensity. Finally, the volatility assessment using
542 thermogram analysis demonstrates WALL-E's capability to retrieve T_{50} values with high
543 precision, aligning well with predicted SIMPOL volatility. Future studies should focus on
544 systematically characterizing SOA volatilities across a broader range of precursor compounds
545 and oxidation conditions, leveraging complementary mass spectrometry and computational
546 modelling techniques to refine volatility estimation approaches.

547 Overall, WALL-E represents a useful and promising tool for atmospheric research, bridging
548 important gaps in real-time aerosol characterization, quantification of chemical composition of
549 complex particulate organic mixtures, and volatility assessment. It improves the time resolution
550 and minimizes measurement artifacts notably due to thermal fragmentation, providing a new
551 technique for investigating the real-time changes in the formation and growth of atmospheric
552 particles for laboratory and field observations.

553 **Data availability**

554 Data of all figures and tables are available on request from the corresponding author.



555 **Author contributions**

556 MR, SP, IZ, MD, and FB designed and built the WALL-E. LG, IZ, ES, CC, and FSD conducted
557 the experiments. LG, IZ, ES, and FSD analyzed the data. IZ did the simulation. LG and IZ
558 prepared the paper with contributions from all co-authors.

559 **Competing interests**

560 The authors declare no competing financial interest.

561 **Acknowledgement**

562 The authors thank Dr. Siegfried Schobesberger for discussing and sharing the FIGAERO
563 measurements and Dr. Georgios Gkatzelis for discussing the declustering scan.

564 **Financial support**

565 This work is funded by the European Research Council Grant (ERC-StG MAARvEL; 423 No.
566 852161). IZ acknowledges funding from the CLOUD-DOC project (Grant Agreement No.
567 101073026) under the HORIZON-MSCA-2021-DN-01 program.

568



569 References

- 570 Bannan, T. J., Le Breton, M., Priestley, M., Worrall, S. D., Bacak, A., Marsden, N. A., Mehra, A., Hammes,
571 J., Hallquist, M., Alfarra, M. R., Krieger, U. K., Reid, J. P., Jayne, J., Robinson, W., McFiggans, G., Coe, H.,
572 Percival, C. J., and Topping, D.: A method for extracting calibrated volatility information from the
573 FIGAERO-HR-ToF-CIMS and its experimental application, *Atmos. Meas. Tech.*, 12, 1429-1439,
574 10.5194/amt-12-1429-2019, 2019.
- 575 Bell, D. M., Zhang, J., Top, J., Bogler, S., Surdu, M., Slowik, J. G., Prevot, A. S. H., and El Haddad, I.:
576 Sensitivity Constraints of Extractive Electrospray for a Model System and Secondary Organic Aerosol,
577 *Analytical Chemistry*, 95, 13788-13795, 10.1021/acs.analchem.3c00441, 2023.
- 578 Bi, C., Krechmer, J. E., Canagaratna, M. R., and Isaacman-VanWertz, G.: Correcting bias in log-linear
579 instrument calibrations in the context of chemical ionization mass spectrometry, *Atmos. Meas. Tech.*,
580 14, 6551-6560, 10.5194/amt-14-6551-2021, 2021.
- 581 Buchholz, A., Ylisirniö, A., Huang, W., Mohr, C., Canagaratna, M., Worsnop, D. R., Schobesberger, S.,
582 and Virtanen, A.: Deconvolution of FIGAERO-CIMS thermal desorption profiles using positive matrix
583 factorisation to identify chemical and physical processes during particle evaporation, *Atmos. Chem.*
584 *Phys.*, 20, 7693-7716, 10.5194/acp-20-7693-2020, 2020.
- 585 Cai, R., Li, Y., Clément, Y., Li, D., Dubois, C., Fabre, M., Besson, L., Perrier, S., George, C., Ehn, M., Huang,
586 C., Yi, P., Ma, Y., and Riva, M.: Orbitool: a software tool for analyzing online Orbitrap mass spectrometry
587 data, *Atmos. Meas. Tech.*, 14, 2377-2387, 10.5194/amt-14-2377-2021, 2021.
- 588 Charnawskas, J. C., Alpert, P. A., Lambe, A. T., Berkemeier, T., O'Brien, R. E., Massoli, P., Onasch, T. B.,
589 Shiraiwa, M., Moffet, R. C., Gilles, M. K., Davidovits, P., Worsnop, D. R., and Knopf, D. A.: Condensed-
590 phase biogenic-anthropogenic interactions with implications for cold cloud formation, *Faraday*
591 *Discussions*, 200, 165-194, 10.1039/C7FD00010C, 2017.
- 592 Compornolle, S., Ceulemans, K., and Müller, J. F.: EVAPORATION: a new vapour pressure estimation
593 method for organic molecules including non-additivity and intramolecular interactions, *Atmos. Chem.*
594 *Phys.*, 11, 9431-9450, 10.5194/acp-11-9431-2011, 2011.
- 595 Du, M., Voliotis, A., Shao, Y., Wang, Y., Bannan, T. J., Pereira, K. L., Hamilton, J. F., Percival, C. J., Alfarra,
596 M. R., and McFiggans, G.: Combined application of online FIGAERO-CIMS and offline LC-Orbitrap mass
597 spectrometry (MS) to characterize the chemical composition of secondary organic aerosol (SOA) in
598 smog chamber studies, *Atmos. Meas. Tech.*, 15, 4385-4406, 10.5194/amt-15-4385-2022, 2022.
- 599 Eichler, P., Müller, M., D'Anna, B., and Wisthaler, A.: A novel inlet system for online chemical analysis
600 of semi-volatile submicron particulate matter, *Atmos. Meas. Tech.*, 8, 1353-1360, 10.5194/amt-8-
601 1353-2015, 2015.
- 602 Fehsenfeld, F., Calvert, J., Fall, R., Goldan, P., Guenther, A. B., Hewitt, C. N., Lamb, B., Liu, S., Trainer,
603 M., Westberg, H., and Zimmerman, P.: Emissions of volatile organic compounds from vegetation and
604 the implications for atmospheric chemistry, *Global Biogeochemical Cycles*, 6, 389-430,
605 <https://doi.org/10.1029/92GB02125>, 1992.
- 606 Häkkinen, E., Zhao, J., Graeffe, F., Fauré, N., Krechmer, J. E., Worsnop, D., Timonen, H., Ehn, M., and
607 Kangasluoma, J.: Online measurement of highly oxygenated compounds from organic aerosol, *Atmos.*
608 *Meas. Tech.*, 16, 1705-1721, 10.5194/amt-16-1705-2023, 2023.
- 609 Iyer, S., Lopez-Hilfiker, F., Lee, B. H., Thornton, J. A., and Kurtén, T.: Modeling the Detection of Organic
610 and Inorganic Compounds Using Iodide-Based Chemical Ionization, *The Journal of Physical Chemistry*
611 *A*, 120, 576-587, 10.1021/acs.jpca.5b09837, 2016.
- 612 Jimenez, J. L., Canagaratna, M. R., Donahue, N. M., Prevot, A. S. H., Zhang, Q., Kroll, J. H., DeCarlo, P.
613 F., Allan, J. D., Coe, H., Ng, N. L., Aiken, A. C., Docherty, K. S., Ulbrich, I. M., Grieshop, A. P., Robinson,
614 A. L., Duplissy, J., Smith, J. D., Wilson, K. R., Lanz, V. A., Hueglin, C., Sun, Y. L., Tian, J., Laaksonen, A.,
615 Raatikainen, T., Rautiainen, J., Vaattovaara, P., Ehn, M., Kulmala, M., Tomlinson, J. M., Collins, D. R.,
616 Cubison, M. J., E., Dunlea, J., Huffman, J. A., Onasch, T. B., Alfarra, M. R., Williams, P. I., Bower, K.,
617 Kondo, Y., Schneider, J., Drewnick, F., Borrmann, S., Weimer, S., Demerjian, K., Salcedo, D., Cottrell, L.,
618 Griffin, R., Takami, A., Miyoshi, T., Hatakeyama, S., Shimono, A., Sun, J. Y., Zhang, Y. M., Dzepina, K.,
619 Kimmel, J. R., Sueper, D., Jayne, J. T., Herndon, S. C., Trimborn, A. M., Williams, L. R., Wood, E. C.,



- 620 Middlebrook, A. M., Kolb, C. E., Baltensperger, U., and Worsnop, D. R.: Evolution of Organic Aerosols
621 in the Atmosphere, *Science*, 326, 1525-1529, doi:10.1126/science.1180353, 2009.
- 622 Kahnt, A., Vermeylen, R., Iinuma, Y., Safi Shalamzari, M., Maenhaut, W., and Claeys, M.: High-
623 molecular-weight esters in α -pinene ozonolysis secondary organic aerosol: structural characterization
624 and mechanistic proposal for their formation from highly oxygenated molecules, *Atmos. Chem. Phys.*,
625 18, 8453-8467, 10.5194/acp-18-8453-2018, 2018.
- 626 Kanakidou, M., Seinfeld, J. H., Pandis, S. N., Barnes, I., Dentener, F. J., Facchini, M. C., Van Dingenen,
627 R., Ervens, B., Nenes, A., Nielsen, C. J., Swietlicki, E., Putaud, J. P., Balkanski, Y., Fuzzi, S., Horth, J.,
628 Moortgat, G. K., Winterhalter, R., Myhre, C. E. L., Tsigaridis, K., Vignati, E., Stephanou, E. G., and Wilson,
629 J.: Organic aerosol and global climate modelling: a review, *Atmos. Chem. Phys.*, 5, 1053-1123,
630 10.5194/acp-5-1053-2005, 2005.
- 631 Kim, H., Barkey, B., and Paulson, S. E.: Real refractive indices of α - and β -pinene and toluene secondary
632 organic aerosols generated from ozonolysis and photo-oxidation, *Journal of Geophysical Research:*
633 *Atmospheres*, 115, <https://doi.org/10.1029/2010JD014549>, 2010.
- 634 Krieger, U. K., Siegrist, F., Marcolli, C., Emanuelsson, E. U., Gøbel, F. M., Bilde, M., Marsh, A., Reid, J. P.,
635 Huisman, A. J., Riipinen, I., Hyttinen, N., Myllys, N., Kurtén, T., Bannan, T., Percival, C. J., and Topping,
636 D.: A reference data set for validating vapor pressure measurement techniques: homologous series of
637 polyethylene glycols, *Atmos. Meas. Tech.*, 11, 49-63, 10.5194/amt-11-49-2018, 2018.
- 638 Kurtén, T., Tiusanen, K., Roldin, P., Rissanen, M., Luy, J.-N., Boy, M., Ehn, M., and Donahue, N.: α -Pinene
639 Autoxidation Products May Not Have Extremely Low Saturation Vapor Pressures Despite High O:C
640 Ratios, *The Journal of Physical Chemistry A*, 120, 2569-2582, 10.1021/acs.jpca.6b02196, 2016.
- 641 Laothawornkitkul, J., Taylor, J. E., Paul, N. D., and Hewitt, C. N.: Biogenic volatile organic compounds in
642 the Earth system, *The New phytologist*, 183, 27-51, 10.1111/j.1469-8137.2009.02859.x, 2009.
- 643 Lee, B. H., Lopez-Hilfiker, F. D., Mohr, C., Kurtén, T., Worsnop, D. R., and Thornton, J. A.: An Iodide-
644 Adduct High-Resolution Time-of-Flight Chemical-Ionization Mass Spectrometer: Application to
645 Atmospheric Inorganic and Organic Compounds, *Environmental Science & Technology*, 48, 6309-6317,
646 10.1021/es500362a, 2014.
- 647 Lee, C. P., Riva, M., Wang, D., Tomaz, S., Li, D., Perrier, S., Slowik, J. G., Bourgain, F., Schmale, J., Prevot,
648 A. S. H., Baltensperger, U., George, C., and El Haddad, I.: Online Aerosol Chemical Characterization by
649 Extractive Electrospray Ionization-Ultrahigh-Resolution Mass Spectrometry (EESI-Orbitrap),
650 *Environmental Science & Technology*, 54, 3871-3880, 10.1021/acs.est.9b07090, 2020.
- 651 Li, H., Almeida, T. G., Luo, Y., Zhao, J., Palm, B. B., Daub, C. D., Huang, W., Mohr, C., Krechmer, J. E.,
652 Kurtén, T., and Ehn, M.: Fragmentation inside proton-transfer-reaction-based mass spectrometers
653 limits the detection of ROOR and ROOH peroxides, *Atmos. Meas. Tech.*, 15, 1811-1827, 10.5194/amt-
654 15-1811-2022, 2022.
- 655 Li, X., Li, Y., Lawler, M. J., Hao, J., Smith, J. N., and Jiang, J.: Composition of Ultrafine Particles in Urban
656 Beijing: Measurement Using a Thermal Desorption Chemical Ionization Mass Spectrometer,
657 *Environmental Science & Technology*, 55, 2859-2868, 10.1021/acs.est.0c06053, 2021.
- 658 Li, Y., Pöschl, U., and Shiraiwa, M.: Molecular corridors and parameterizations of volatility in the
659 chemical evolution of organic aerosols, *Atmos. Chem. Phys.*, 16, 3327-3344, 10.5194/acp-16-3327-
660 2016, 2016.
- 661 Lopez-Hilfiker, F. D., Iyer, S., Mohr, C., Lee, B. H., D'Ambro, E. L., Kurtén, T., and Thornton, J. A.:
662 Constraining the sensitivity of iodide adduct chemical ionization mass spectrometry to multifunctional
663 organic molecules using the collision limit and thermodynamic stability of iodide ion adducts, *Atmos.*
664 *Meas. Tech.*, 9, 1505-1512, 10.5194/amt-9-1505-2016, 2016.
- 665 Lopez-Hilfiker, F. D., Pospisilova, V., Huang, W., Kalberer, M., Mohr, C., Stefenelli, G., Thornton, J. A.,
666 Baltensperger, U., Prevot, A. S. H., and Slowik, J. G.: An extractive electrospray ionization time-of-flight
667 mass spectrometer (EESI-TOF) for online measurement of atmospheric aerosol particles, *Atmos. Meas.*
668 *Tech.*, 12, 4867-4886, 10.5194/amt-12-4867-2019, 2019.
- 669 Lopez-Hilfiker, F. D., Mohr, C., Ehn, M., Rubach, F., Kleist, E., Wildt, J., Mentel, T. F., Lutz, A., Hallquist,
670 M., Worsnop, D., and Thornton, J. A.: A novel method for online analysis of gas and particle



- 671 composition: description and evaluation of a Filter Inlet for Gases and AEROSols (FIGAERO), *Atmos.*
672 *Meas. Tech.*, 7, 983-1001, 10.5194/amt-7-983-2014, 2014.
- 673 Mellouki, A., Wallington, T. J., and Chen, J.: Atmospheric Chemistry of Oxygenated Volatile Organic
674 Compounds: Impacts on Air Quality and Climate, *Chemical Reviews*, 115, 3984-4014,
675 10.1021/cr500549n, 2015.
- 676 Müller, M., Eichler, P., D'Anna, B., Tan, W., and Wisthaler, A.: Direct Sampling and Analysis of
677 Atmospheric Particulate Organic Matter by Proton-Transfer-Reaction Mass Spectrometry, *Analytical*
678 *Chemistry*, 89, 10889-10897, 10.1021/acs.analchem.7b02582, 2017.
- 679 Pai, S. J., Heald, C. L., Pierce, J. R., Farina, S. C., Marais, E. A., Jimenez, J. L., Campuzano-Jost, P., Nault,
680 B. A., Middlebrook, A. M., Coe, H., Shilling, J. E., Bahreini, R., Dingle, J. H., and Vu, K.: An evaluation of
681 global organic aerosol schemes using airborne observations, *Atmos. Chem. Phys.*, 20, 2637-2665,
682 10.5194/acp-20-2637-2020, 2020.
- 683 Peng, Y., Wang, H., Gao, Y., Jing, S., Zhu, S., Huang, D., Hao, P., Lou, S., Cheng, T., Huang, C., and Zhang,
684 X.: Real-time measurement of phase partitioning of organic compounds using a proton-transfer-
685 reaction time-of-flight mass spectrometer coupled to a CHARON inlet, *Atmos. Meas. Tech.*, 16, 15-28,
686 10.5194/amt-16-15-2023, 2023.
- 687 Peräkylä, O., Riva, M., Heikkinen, L., Quéléver, L., Roldin, P., and Ehn, M.: Experimental investigation
688 into the volatilities of highly oxygenated organic molecules (HOMs), *Atmos. Chem. Phys.*, 20, 649-669,
689 10.5194/acp-20-649-2020, 2020.
- 690 Riva, M., Brüggemann, M., Li, D., Perrier, S., George, C., Herrmann, H., and Berndt, T.: Capability of CI-
691 Orbitrap for Gas-Phase Analysis in Atmospheric Chemistry: A Comparison with the CI-API-TOF
692 Technique, *Analytical Chemistry*, 92, 8142-8150, 10.1021/acs.analchem.0c00111, 2020.
- 693 Riva, M., Ehn, M., Li, D., Tomaz, S., Bourgain, F., Perrier, S., and George, C.: CI-Orbitrap: An Analytical
694 Instrument To Study Atmospheric Reactive Organic Species, *Analytical Chemistry*, 91, 9419-9423,
695 10.1021/acs.analchem.9b02093, 2019a.
- 696 Riva, M., Rantala, P., Krechmer, J. E., Peräkylä, O., Zhang, Y., Heikkinen, L., Garmash, O., Yan, C., Kulmala,
697 M., Worsnop, D., and Ehn, M.: Evaluating the performance of five different chemical ionization
698 techniques for detecting gaseous oxygenated organic species, *Atmos. Meas. Tech.*, 12, 2403-2421,
699 10.5194/amt-12-2403-2019, 2019b.
- 700 Schobesberger, S., D'Ambro, E. L., Lopez-Hilfiker, F. D., Mohr, C., and Thornton, J. A.: A model
701 framework to retrieve thermodynamic and kinetic properties of organic aerosol from composition-
702 resolved thermal desorption measurements, *Atmos. Chem. Phys.*, 18, 14757-14785, 10.5194/acp-18-
703 14757-2018, 2018.
- 704 Shilling, J. E., Chen, Q., King, S. M., Rosenoern, T., Kroll, J. H., Worsnop, D. R., DeCarlo, P. F., Aiken, A.
705 C., Sueper, D., Jimenez, J. L., and Martin, S. T.: Loading-dependent elemental composition of α -pinene
706 SOA particles, *Atmos. Chem. Phys.*, 9, 771-782, 10.5194/acp-9-771-2009, 2009.
- 707 Smith, J. N., Moore, K. F., McMurry, P. H., and Eisele, F. L.: Atmospheric Measurements of Sub-20 nm
708 Diameter Particle Chemical Composition by Thermal Desorption Chemical Ionization Mass
709 Spectrometry, *Aerosol Science and Technology*, 38, 100-110, 10.1080/02786820490249036, 2004.
- 710 Song, M., He, S., Li, X., Liu, Y., Lou, S., Lu, S., Zeng, L., and Zhang, Y.: Optimizing the iodide-adduct
711 chemical ionization mass spectrometry (CIMS) quantitative method for toluene oxidation
712 intermediates: experimental insights into functional-group differences, *Atmos. Meas. Tech.*, 17, 5113-
713 5127, 10.5194/amt-17-5113-2024, 2024.
- 714 Stark, H., Yatavelli, R. L. N., Thompson, S. L., Kang, H., Krechmer, J. E., Kimmel, J. R., Palm, B. B., Hu, W.,
715 Hayes, P. L., Day, D. A., Campuzano-Jost, P., Canagaratna, M. R., Jayne, J. T., Worsnop, D. R., and
716 Jimenez, J. L.: Impact of Thermal Decomposition on Thermal Desorption Instruments: Advantage of
717 Thermogram Analysis for Quantifying Volatility Distributions of Organic Species, *Environmental*
718 *Science & Technology*, 51, 8491-8500, 10.1021/acs.est.7b00160, 2017.
- 719 Stein, S. E. and Scott, D. R.: Optimization and testing of mass spectral library search algorithms for
720 compound identification, *Journal of the American Society for Mass Spectrometry*, 5, 859-866,
721 10.1016/1044-0305(94)87009-8, 1994.



- 722 Thornton, J. A., Mohr, C., Schobesberger, S., D'Ambro, E. L., Lee, B. H., and Lopez-Hilfiker, F. D.:
723 Evaluating Organic Aerosol Sources and Evolution with a Combined Molecular Composition and
724 Volatility Framework Using the Filter Inlet for Gases and Aerosols (FIGAERO), *Accounts of Chemical*
725 *Research*, 53, 1415-1426, 10.1021/acs.accounts.0c00259, 2020.
- 726 Tikkanen, O. P., Buchholz, A., Ylisirniö, A., Schobesberger, S., Virtanen, A., and Yli-Juuti, T.: Comparing
727 secondary organic aerosol (SOA) volatility distributions derived from isothermal SOA particle
728 evaporation data and FIGAERO-CIMS measurements, *Atmos. Chem. Phys.*, 20, 10441-10458,
729 10.5194/acp-20-10441-2020, 2020.
- 730 Vogel, A. L., Schneider, J., Müller-Tautges, C., Klimach, T., and Hoffmann, T.: Aerosol Chemistry
731 Resolved by Mass Spectrometry: Insights into Particle Growth after Ambient New Particle Formation,
732 *Environmental Science & Technology*, 50, 10814-10822, 10.1021/acs.est.6b01673, 2016.
- 733 Voisin, D., Smith, J. N., Sakurai, H., McMurry, P. H., and Eisele, F. L.: Thermal Desorption Chemical
734 Ionization Mass Spectrometer for Ultrafine Particle Chemical Composition, *Aerosol Science and*
735 *Technology*, 37, 471-475, 10.1080/02786820300959, 2003.
- 736 Wang, D. S., Lee, C. P., Krechmer, J. E., Majluf, F., Tong, Y., Canagaratna, M. R., Schmale, J., Prévôt, A.
737 S. H., Baltensperger, U., Dommén, J., El Haddad, I., Slowik, J. G., and Bell, D. M.: Constraining the
738 response factors of an extractive electrospray ionization mass spectrometer for near-molecular
739 aerosol speciation, *Atmos. Meas. Tech.*, 14, 6955-6972, 10.5194/amt-14-6955-2021, 2021.
- 740 Wilson, J., Imre, D., Beránek, J., Shrivastava, M., and Zelenyuk, A.: Evaporation Kinetics of Laboratory-
741 Generated Secondary Organic Aerosols at Elevated Relative Humidity, *Environmental Science &*
742 *Technology*, 49, 243-249, 10.1021/es505331d, 2015.
- 743 Witkowski, B., al-Sharafi, M., Błaziak, K., and Gierczak, T.: Aging of α -Pinene Secondary Organic Aerosol
744 by Hydroxyl Radicals in the Aqueous Phase: Kinetics and Products, *Environmental Science &*
745 *Technology*, 57, 6040-6051, 10.1021/acs.est.2c07630, 2023.
- 746 Wong, C., Liu, S., and Nizkorodov, S. A.: Highly Acidic Conditions Drastically Alter the Chemical
747 Composition and Absorption Coefficient of α -Pinene Secondary Organic Aerosol, *ACS Earth and Space*
748 *Chemistry*, 6, 2983-2994, 10.1021/acsearthspacechem.2c00249, 2022.
- 749 Xu, L., Coggon, M. M., Stockwell, C. E., Gilman, J. B., Robinson, M. A., Breitenlechner, M., Lamplugh, A.,
750 Crounse, J. D., Wennberg, P. O., Neuman, J. A., Novak, G. A., Veres, P. R., Brown, S. S., and Warneke,
751 C.: Chemical ionization mass spectrometry utilizing ammonium ions (NH_4^+ CIMS) for measurements
752 of organic compounds in the atmosphere, *Atmos. Meas. Tech.*, 15, 7353-7373, 10.5194/amt-15-7353-
753 2022, 2022.
- 754 Yang, Z., Zhou, D.-D., Huang, S.-Y., Fang, A.-P., Li, H.-B., and Zhu, H.-L.: Effects and mechanisms of
755 natural products on Alzheimer's disease, *Critical Reviews in Food Science and Nutrition*, 63, 3168-3188,
756 10.1080/10408398.2021.1985428, 2023.
- 757 Ylisirniö, A., Barreira, L. M. F., Pullinen, I., Buchholz, A., Jayne, J., Krechmer, J. E., Worsnop, D. R.,
758 Virtanen, A., and Schobesberger, S.: On the calibration of FIGAERO-ToF-CIMS: importance and impact
759 of calibrant delivery for the particle-phase calibration, *Atmos. Meas. Tech.*, 14, 355-367, 10.5194/amt-
760 14-355-2021, 2021.
- 761 Zaytsev, A., Breitenlechner, M., Koss, A. R., Lim, C. Y., Rowe, J. C., Kroll, J. H., and Keutsch, F. N.: Using
762 collision-induced dissociation to constrain sensitivity of ammonia chemical ionization mass
763 spectrometry (NH_4^+ CIMS) to oxygenated volatile organic compounds, *Atmos. Meas. Tech.*, 12, 1861-
764 1870, 10.5194/amt-12-1861-2019, 2019.
- 765 Zhang, X., McVay, R. C., Huang, D. D., Dalleska, N. F., Aumont, B., Flagan, R. C., and Seinfeld, J. H.:
766 Formation and evolution of molecular products in α -pinene secondary organic aerosol, *Proceedings of*
767 *the National Academy of Sciences*, 112, 14168-14173, doi:10.1073/pnas.1517742112, 2015.
- 768 Zhao, J., Häkkinen, E., Graeffe, F., Krechmer, J. E., Canagaratna, M. R., Worsnop, D. R., Kangasluoma,
769 J., and Ehn, M.: A combined gas- and particle-phase analysis of highly oxygenated organic molecules
770 (HOMs) from α -pinene ozonolysis, *Atmos. Chem. Phys.*, 23, 3707-3730, 10.5194/acp-23-3707-2023,
771 2023.



772 Zhao, J., Mickwitz, V., Zhang, J., Alton, M., Canagaratna, M., Graeffe, F., Schobesberger, S., Worsnop,
773 D., and Ehn, M.: Comparison of Gaseous and Particulate Highly Oxygenated Organic Molecules from
774 the Ozonolysis of Terpenes, *ACS ES&T Air*, 1, 1294-1303, 10.1021/acsestair.4c00121, 2024a.
775 Zhao, J., Mickwitz, V., Luo, Y., Häkkinen, E., Graeffe, F., Zhang, J., Timonen, H., Canagaratna, M.,
776 Krechmer, J. E., Zhang, Q., Kulmala, M., Kangasluoma, J., Worsnop, D., and Ehn, M.: Characterization
777 of the Vaporization Inlet for Aerosols (VIA) for online measurements of particulate highly oxygenated
778 organic molecules (HOMs), *Atmos. Meas. Tech.*, 17, 1527-1543, 10.5194/amt-17-1527-2024, 2024b.
779 Zuth, C., Vogel, A. L., Ockenfeld, S., Huesmann, R., and Hoffmann, T.: Ultrahigh-Resolution Mass
780 Spectrometry in Real Time: Atmospheric Pressure Chemical Ionization Orbitrap Mass Spectrometry of
781 Atmospheric Organic Aerosol, *Analytical Chemistry*, 90, 8816-8823, 10.1021/acs.analchem.8b00671,
782 2018.

783